Bulletin of the Seismological Society of America, Vol. 84, No. 2, pp. 269–283, April 1994

Wide-Band Analysis of the 3 March 1985 Central Chile Earthquake: Overall Source Process and Rupture History

by Carlos Mendoza, Stephen Hartzell, and Tony Monfret

Abstract We apply a linear, finite-fault waveform inversion scheme to the near-source strong-motion records, the teleseismic body waves, and the long-period Rayleigh waves recorded for the 3 March 1985 Chile earthquake to recover the mainshock rupture history. The data contain periods between about 2 and 350 sec and are inverted by allowing a variable dislocation rise time at each point on the fault. The results indicate that the mainshock had a seismic moment of 1.5×10^{28} dyne-cm (M_w 8.0) and ruptured mainly updip and to the south of the hypocenter for a distance of about 150 km along the Nazca–South America plate boundary. A smaller northward component of propagation is also evident, giving a total rupture length of about 200 km. The total source duration of the mainshock is 70 sec, with the majority of the slip occurring within the first 40 sec in a broad 100-km-wide zone in the northern half of the rupture area. Slip in this region extends from a depth of 55 km to within about 10 km of the surface and contains two areas of maximum slip (2.3 and 2.9 m) with rise times of approximately 14 sec. Slip in the southern portion of the fault reaches lower peak values (1.8 m) and extends downdip to depths no greater than 30 km. An independent variable rise-time inversion of the teleseismic body waves alone yields similar results, indicating that a significant component of slow fault motion is not required for this earthquake. The mainshock was preceded by several smaller precursors, the largest of which is an $M_w \sim 6.6$ thrust earthquake occurring at a depth of 22 km in the shallow 15° dipping portion of the plate interface.

Introduction

The use of finite-fault inversion schemes has become relatively common in the study of large earthquake ruptures. Although the methods vary, the procedure usually involves an inversion of the observed ground-motion records to recover the co-seismic moment release on the fault using a fault orientation prescribed by previously computed centroidal parameters. These inversion methods, which can be linear or nonlinear in approach, have been applied to near-source strong ground motions and teleseismic body-wave observations to identify the spatial and temporal rupture pattern as a function of position on the fault (e.g., Hartzell and Heaton, 1983; Kikuchi and Fukao, 1985; Yoshida, 1986; Fukuyama and Irikura, 1986; Takeo, 1987; Beroza and Spudich, 1988; Hartzell, 1989; Das and Kostrov, 1990). The seismic records are typically dominated by energy at periods below 50 sec. Periods shorter than about 1 sec, however, are usually not considered because they are difficult to model reliably owing to complex propagation-path effects. An inversion technique has also been applied to intermediate-period (10 to 25 sec) Rayleigh waves recorded at regional distances where the effects of lateral crustal-velocity variations are minimized (e.g., Mori and Shimazaki, 1985). The results of these applications indicate that the details of the fault dislocation can be inferred from a direct analysis of seismic waves recorded at relatively short periods (less than 50 sec) and suggest a heterogeneous rupture history characterized by independent source regions separated in both space and time on an earthquake fault.

Seismic data recorded at periods longer than 100 sec are usually not considered in finite-fault studies even though they provide information on the overall size and duration of the earthquake. This is mainly owing to the fact that long-period waveforms have a limited resolution in defining the spatial and temporal details of the source (e.g., Mendoza and Hartzell, 1988). However, seismic-moment and source-duration estimates currently obtained in finite-fault inversions would be underestimated if the earthquake preferentially excites long-pe-

riod surface waves without affecting the body-wave radiation. Recent centroidal studies of some large plate-boundary earthquakes have found a discrepancy in the seismic moments estimated independently from body-wave and surface-wave data, suggesting that frequency-dependent seismic-wave excitation may sometimes occur as a result of an anomalously slow fault-dislocation process (e.g., Anderson and Zhang, 1991). In a long-period (150 to 300 sec) analysis of two large ($M_w > 8.0$) earthquakes, Zhang and Lay (1989) also discovered that source complexity can affect Rayleigh waveforms sufficiently to influence the derivation of centroidal source parameters. This would suggest that long-period Rayleigh waves may also provide constraints on the temporal and spatial pattern of large earthquake rupture when used in conjunction with the body-wave data.

In this study, we apply a linear, point-by-point inversion scheme to long-period Rayleigh waves, in addition to near-source strong motions and teleseismic body waves, to infer the source properties of a large earthquake rupture. The study represents the first application of a formal finite-fault inversion scheme to wide-band seismic-wave data that contain periods greater than 100 sec. In particular, we examine the large 7.8 M_S central Chile earthquake of 3 March 1985. This earthquake occurred within a region of previous great historical subduction earthquakes and may have filled a gap of high seismic potential on the Nazca–South America plate boundary (Nishenko, 1985; Comte *et al.*, 1986). Seismic moments previously estimated for the earthquake vary with the frequency content of the data utilized (see Table 1). The moment calculated using surface waves and geodetic data are consistently greater than that determined using teleseismic body waves. This discrepancy in estimated moment may suggest that the 1985 Chile earthquake involved a slow component of fault slip that radiated little or no body-wave energy.

Moment-tensor inversions of long-period surface waves (Dziewonski *et al.*, 1985; Monfret and Romanowicz, 1986; Zhang and Kanamori, 1988a) require a source centroid with a thrust mechanism consistent with shallow-angle subduction (Table 1). Choy and Dewey (1988) obtain a similar mechanism from forward modeling the broadband teleseismic *P* waves. Centroidal analyses of the recorded *P* waves (Christensen and Ruff, 1986; Choy and Dewey, 1988) and long-period Rayleigh waves (Monfret and Romanowicz, 1986; Zhang and Kanamori, 1988b) indicate that the rupture propagated southward from the hypocenter. The rupture lengths estimated from these data, however, appear to be frequency dependent, similar to the seismic moment (see Table 1). The *P* waves suggest rupture lengths of 75 to 90 km, whereas the long-period Rayleigh waves indicate lengths of 100 to 150 km. The geodetic data prefer an

Table 1
Source Properties of the 3 March 1985 Chile Earthquake

Data*	θ (°)	δ (°)	ψ (°)	Depth (km)	M_0†	L‡ (km)	τ§ (sec)
[1]Geodetic Deformation	10¶	18	105¶	20–60	1.6	250#	—
[2]GEOSCOPE/IDA Rayleigh Waves	10	25	110	60**	1.2	100	60–80
[3]GDSN/IDA Rayleigh Waves	4	21	95	44**	1.2	150	69
[4]GDSN *LP* Body and Surface Waves	11	26	110	41**	1.0	—	69
[5]GDSN *IP*, *LP P* Waves	11¶	26¶	110¶	20–50	1.0¶	120	—
[6]GDSN *BB*, *IP*, *LP P* Waves	10¶	30¶	105¶	5–35	—	180#	60
[7]GDSN *BB P* Waves	360	35	105	34–46	0.4	90	—
[8]WWSSN *LP P* Waves	11¶	26¶	110¶	10–40	0.7	75	—
[9]WWSSN *LP P* Waves	—	—	—	—	0.3	—	40
[10]GDSN *BB*, *IP*, *LP* Body Waves; GEOSCOPE/IDA Rayleigh Waves; Strong Motions	5¶	15¶,30¶	90¶,110¶	10–55	1.5	200#	70

*The superior numbers in this column refer to the following references: [1]Barrientos (1988); [2]Monfret and Romanowicz (1986); [3]Zhang and Kanamori (1988a; 1988b); [4]Dziewonski *et al.* (1985); [5]Yoshida (1992); [6]Houston and Kanamori (1990); [7]Choy and Dewey (1988); [8]Christensen and Ruff (1986); [9]Korrat and Madariaga (1986); [10]this study.

†Seismic moment in units of 10^{28} dyne-cm.

‡Rupture length.

§Mainshock duration.

¶Fixed in computation.

#Bilateral rupture.

**Centroid depth.

even greater rupture length of about 250 km (Barrientos, 1988).

The depth extent of faulting during the 1985 Chile earthquake is also not well constrained. Previous estimates cover different depth ranges between 5 and 60 km with the body waves favoring depths shallower than 40 km (Table 1). The long-period surface-wave centroid depths would suggest that the Rayleigh-wave data resolve a deeper rupture extent further downdip than indicated by the teleseismic *P* waves. If so, then the discrepancy in seismic moment might be explained by an anomalously slow dislocation process in the downdip portion of the plate interface that would preferentially excite the long-period seismic waves without introducing additional moment to the recorded body waveforms. This mechanism of faulting has been proposed by Anderson and Zhang (1991) for the large 1989 Macquarie Ridge strike-slip plate-boundary earthquake and has been suggested for the 1985 Chile earthquake by Zhang and Kanamori (1988a). We examine this hypothesis using the very broad frequency content present in our data set. Our results, however, indicate that a single rupture model with a variable dislocation rise time can explain the entire suite of observations well, and it is not necessary to introduce a significant component of slower fault motion to reconcile the long-period Rayleigh-wave amplitudes.

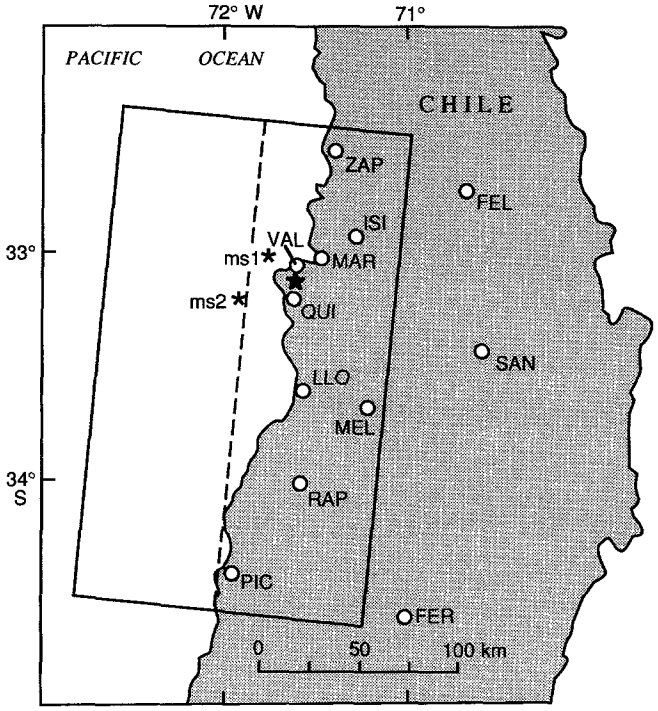

Figure 1. Geographic map of central Chile showing the epicentral locations of the main-rupture nucleation point (star) and precursory subevents *ms*1 and *ms*2 of the 3 March 1985 Chile earthquake (from Choy and Dewey, 1988). Circles denote strong-motion sites, and the rectangle is the surface projection of the fault plane used in our final analysis of the seismic-wave data. The dashed line indicates where the fault dip changes landward from 15° to 30°.

Table 2
Strong-Motion Stations

Station	Code	Latitude (°S)	Longitude (°W)	Components
Santiago	SAN	33.45	70.67	0,Up,90
Melipilla	MEL	33.68	71.22	0,Up,90
Pichilemu	PIC	34.38	72.02	0,Up,90
Quintay	QUI	33.20	71.68	90,Up,0
Rapel	RAP	34.03	71.58	0,Up,90
San Fernando	FER	34.60	71.00	0,Up,90
San Isidro	ISI	32.90	71.27	0,Up,90
Zapallar	ZAP	32.57	71.47	0,Up,90
San Felipe	FEL	32.75	70.73	170,Up,80
Llolleo	LLO	33.58	71.61	100,Up,10
Vina Del Mar	MAR	33.03	71.58	290,Up,200
Valparaiso	VAL	33.08	71.63	160,Up,70

Seismic Waveform Data

The 1985 Chile earthquake is characterized by a series of multiple events that are well separated in time in the recorded *P* waveforms (e.g., Christensen and Ruff, 1986; Korrat and Madariaga, 1986; Choy and Dewey, 1988). Choy and Dewey (1988) identify three distinct *P* arrivals in the Global Digital Seismograph Network (GDSN) waveforms, including two precursory phases (*ms*1 and *ms*2) prior to the mainshock (*MS*). The *ms*2 arrival, which occurs 16 to 18 sec before the *MS* onset, was initially interpreted as the mainshock (e.g., Korrat and Madariaga, 1986), but *MS* clearly corresponds to the major moment release during the earthquake (Choy and Dewey, 1988) and is the principal contributor to the observed long-period Rayleigh waveforms. The *MS* is located on the Nazca–South America plate interface at a depth of 40 km (Choy and Dewey, 1988). The *ms*1 and *ms*2 epicenters are seaward of the *MS* hypocenter (see Fig. 1), consistent with occurrence in the updip portion of the plate boundary. Focal depths for *ms*1 and *ms*2, however, cannot be accurately estimated from the observed differential arrival times (Choy and Dewey, 1988).

Figure 1 also shows the local strong-motion stations used in our study. These stations are listed in Table 2. Uncorrected accelerograms came from two sources: Empresa Nacional de Electricidad (ENDESA) and the Department of Geology and Geophysics of the University of Chile (Celebi, 1987; Campbell *et al.*, 1989). Inaccuracies in digitization resulted in large baseline errors for many of the records. Multiple piecewise baseline corrections were applied to the acceleration records to recover as long a period content as possible. The accelerograms were then corrected for the response of the instrument and integrated to velocity. Many of the strong-motion records exhibit a predominantly high-frequency

content (greater than 1 Hz) and a ringing character indicating significant site effects. Stations with strong site effects were not used in the inversion. Velocity records from the remaining sites were bandpass-filtered with a Butterworth filter (Oppenheim and Schafer, 1975) from 2.0 to 7.5 sec. This passband was judged to yield the most accurately modelable ground motion given our limited knowledge of the local velocity structure. The velocity records were then resampled at a time step of 0.2 sec (Nyquist frequency of 2.5 Hz) for the inversion.

Body- and surface-wave records used in the inversion are listed in Table 3. These include teleseismic *P* and *SH* waveforms recorded by the GDSN and long-period *R*1, *R*2, and *R*3 vertical Rayleigh waves recorded at very long periods by the GEOSCOPE and IDA (International Deployment of Accelerometers) networks. Teleseismic GDSN *P* waves recorded at distances between 27° and 125° were considered for inversion. Teleseismic distances considered for *SH* waves range from 40° to 100°. Because body-wave amplitudes may be significantly reduced at large distances as a result of core diffractions, however, we downweighted *P* waveforms beyond 110° and *SH* waves recorded at distances greater than 90°. The character of the these downweighted records is similar to those receiving full weight in the inversion, and we believe that any errors introduced by including the more distant stations are small and outweighed by the increased azimuthal coverage. Whenever available, we used the intermediate-period channel of the GDSN body-wave data to be inverted. For five of the GDSN stations, however, both short- and long-period records are available, allowing us to reconstruct vertical broadband *P* waveforms using the procedure described by Harvey and Choy (1982). These reconstructed waveforms contain ground displacement for frequencies between 0.01 and 5.0 Hz. Long-period, vertical *P* waveforms were also included for those GDSN stations lacking short- and intermediate-period channels. Except for station RSSD, where a maximum of 70 sec was available, body-wave record lengths of 100 sec were selected for analysis. The intermediate-period and broadband waveforms have a 0.25-sec sampling interval, and the long-period records are sampled once every second.

We used only the three Rayleigh wave trains (*R*1, *R*2, and *R*3) to minimize travel-path effects in modeling the dynamics of the source (Monfret and Romanowicz, 1986). These wave trains were generally available for the GEOSCOPE stations. The *R*1 waves recorded by the IDA network were off-scale and were not included. We used the variable-filter algorithm of Cara (1973) to select the Rayleigh fundamental mode, thereby eliminating overtone contamination and increasing the signal-to-noise ratio. This filtering process can result in amplitude perturbations to the fundamental mode; however, the perturbations are relatively small (less than 2%) and do not affect our analysis of the earthquake source. We could not properly recover the *R*1 fundamental mode for GEOSCOPE station WFM and thus did not include it in the inversion. The Rayleigh records are sampled once every 10 sec and have been bandpass-filtered at periods between 100 and 350 sec using an 8-pole Butterworth filter. Record lengths vary from station to station but have generally been set to about 20, 35, and 70 min for *R*1, *R*2, and *R*3 wave trains, respectively.

Table 3
Teleseismic and Surface-Wave Stations

Network	Station	Records	Distance (°)	Azimuth (°)
GDSN	BCAO	*BB P*	92.73	86.52
	GRFO	*BB P*	110.37	43.45
	CTAO	*BB P*	115.76	220.12
	COL	*BB P*	113.89	333.09
	SCP	*BB P, IP SH*	73.77	355.26
	LON	*IP P, IP SH*	91.35	328.23
	SLR	*IP P, IP SH*	84.17	116.82
	TAU	*IP P, IP SH*	96.24	207.84
	RSNY	*IP P, IP SH*	77.35	358.05
	RSON	*IP P, IP SH*	85.82	346.33
	RSSD	*IP P*	82.29	337.24
	BDF	*IP P*	27.80	57.04
	TOL	*IP P*	95.95	45.76
	KEV	*LP P*	123.71	24.42
	AFI	*LP P*	90.59	253.06
	NWAO	*LP P*	113.73	188.36
GEOSCOPE	SSB	*R*1, *R*2, *R*3	104.19	45.13
	PCR	*R*1, *R*2, *R*3	106.04	129.48
	PAF	*R*1, *R*2, *R*3	90.99	156.23
	TAM	*R*1, *R*2, *R*3	92.20	64.37
	WFM	*R*2, *R*3	75.54	00.10
IDA	ESK	*R*2, *R*3	105.77	33.63
	KIP	*R*2, *R*3	98.60	289.70
	PFO	*R*2, *R*3	78.77	323.03
	SUR	*R*2, *R*3	74.86	119.02
	TWO	*R*2, *R*3	106.37	205.40

Finite-Fault Inversion Method

We use the linear point-by-point inversion scheme developed by Hartzell and Heaton (1983; 1986). This technique has since been widely used in the analysis of near-source and teleseismic data (e.g., Mendoza and Hartzell, 1988; 1989; Hartzell and Iida, 1990; Hartzell *et al.*, 1991; Wald *et al.*, 1990; Mendoza, 1993). For a detailed discussion of the method see Hartzell (1989). Briefly, the procedure requires placing a fault plane in the earthquake source region and subdividing it into a finite number of subfaults. Synthetic Green's functions are then generated for each subfault assuming a dislocation rise time of finite duration and a constant propagation of rupture away from the hypocenter. For each subfault, the synthetic waveforms at all stations are joined end to end, forming a large synthetics matrix **A**. The observations are similarly joined in a data vector **b**, resulting in an overdetermined system of linear equations

of the form $\mathbf{A}x = \mathbf{b}$ that can then be solved for x, the dislocation weights required of each subfault to reproduce the observed data. Stability is achieved by imposing a positivity constraint and additional linear constraints of the form $\lambda\mathbf{F}x = \lambda\mathbf{d}$, where λ is a scalar weighting factor. The solution is constrained to have a smooth variation of slip from subfault to subfault by choosing $\mathbf{F}$ and $\mathbf{d}$ such that the weighted difference between adjacent dislocations is zero. Also, the total seismic moment is minimized by letting $\mathbf{F}$ be the identity matrix and $\mathbf{d}$ the zero vector. In practice, several inversion runs must be conducted to identify the proper weighting for smoothing and moment minimization. The proper weighting is given by the largest λ values that allow the observed records to be fit by the synthetics, resulting in the least complicated model for the source.

This fixed-velocity approach can provide an accurate image of the co-seismic slip distribution for simple coherent ruptures. For more complicated events, however, the method may yield incorrect results if flexibility in the rise time and rupture time of the individual subfaults is not allowed. We introduce this flexibility by using a time-window application that allows multiple consecutive slip intervals that discretize the subfault rise time and rupture time. In this alternative approach, the slip function at any point on the fault is approximated by a discrete number of boxcars of fixed duration and variable amplitude. The inversion then solves for the contribution of slip within each time window (the boxcar amplitude) thus allowing for a variable subfault rise time and relaxing the constraints of fixed rupture velocity. This method has been applied previously to several large earthquakes but has generally been restricted to a maximum of three time windows owing to computational limitations (e.g., Hartzell and Heaton, 1983; 1986; Mendoza and Hartzell, 1989). Our current computational capabilities allow us to use up to 14 time windows for the Chile earthquake. Boxcar durations of 1 or 2 sec are used to compute the subfault Green's functions using a maximum rupture velocity of 3 km/sec. This velocity corresponds to the maximum allowable velocity for rupture propagation across the fault.

Teleseismic body-wave Green's functions were obtained by summing individual point-source responses distributed across each subfault. These responses were computed with the generalized ray procedure of Langston and Helmberger (1975), which considers internal reflections within a layered velocity structure and *P*-to-*SV* conversions at the surface and Moho interfaces. Attenuation was included by convolving the synthetics with the frequency-dependent t^* operator obtained by Choy and Cormier (1986) for a surface source. This operator has t^* values for *P* waves that vary from 1 to 0.5 for frequencies from 0.1 to 5 Hz. The t^* values for *S* waves are approximately 4.5 times greater at these same frequencies. Strong-motion synthetics were calculated using the wavenumber integration method of Saikia and Burdick (1991). Ground-motion synthetics were calculated to a Nyquist frequency of 2.5 Hz for a suite of source-to-site ranges and depths. Point-source summation and waveform interpolation (Hartzell and Heaton, 1983) were then used to calculate the response of a finite fault. The strong-motion synthetics were bandpass-filtered with the same Butterworth filter used on the data and resampled at a time step of 0.2 sec. We used local crustal velocities based on the results of Pardo and Fuenzalida (1988) and Kausel and Cruzat (1985) to calculate both strong-motion and teleseismic body-wave synthetics. The crustal structure used to calculate the strong-motion synthetics is given in Table 4. For the teleseismic synthetics, we omitted the top 0.1-km layer, and we combined layers 6 and 7 into a single layer 13-km thick.

Fundamental-mode *R*1, *R*2, and *R*3 synthetic seismograms were calculated using time-domain eigenmode summation (Kanamori and Cipar, 1974) assuming a point source with a step-function dislocation for each subfault. Convolution with the 1- or 2-sec boxcar durations considered here has no measurable effect on the surface-wave synthetics. Surface-wave eigenfunctions and attenuation were obtained from the Preliminary Reference Earth Model (PREM) of Dziewonski and Anderson (1981). The wavelengths of the GEOSCOPE and IDA Rayleigh wave trains examined in this study are greater than 300 km and are not affected by the crustal velocity structure. Thus, it is not necessary to consider near-surface properties to generate the Rayleigh-wave synthetics. Prior to the inversion, the Rayleigh synthetics were bandpass-filtered at periods between 100 and 350 sec, similar to the observed records.

Teleseismic Body-Wave Analysis

We have independently inverted the GDSN body-wave data set described earlier to identify the source properties of the 1985 Chile earthquake that are consistent with seismic-wave periods below 100 sec. Previous finite-fault studies of the earthquake (e.g., Houston and Kanamori, 1990; Yoshida, 1992) have inverted the *P*-wave records

Table 4
Local Crustal Structure

V_P (km/sec)	V_S (km/sec)	Density (g/cm^3)	Thickness (km)	Q_P	Q_S
2.50	1.44	1.60	0.1	60	30
4.00	2.31	1.70	1.0	100	50
4.75	2.74	2.00	3.0	200	100
5.56	3.21	2.30	4.0	400	200
6.07	3.50	2.50	8.9	500	250
6.53	3.77	2.65	5.5	600	300
7.00	4.04	2.80	7.6	600	300
8.00	4.62	3.28	—	1000	500

alone using the *ms*2 arrival times. Yoshida (1992) used a fixed-velocity approach and found that a rupture velocity of 2 km/sec gave the best fit to the observed GDSN *P* waveforms. Our own analysis of both *P* and *SH* body waves using a constant rupture velocity of 2 km/sec and a similar fault geometry (5° strike, 25° dip) yields a similar rupture pattern. The solution (Fig. 2) suggests that rupture began with a relatively small source near the hypocenter followed by the majority of the slip southward and downdip of *ms*2. In our inversion, we compute both strike-slip and dip-slip contributions to the source assuming a triangular rise time of 2 sec. Except for the source near the hypocenter, the vector sum of both components yields a relatively constant 115° rake across the fault. This value is consistent with rakes previously computed for the earthquake (see Table 1) and is similar to the 110° rake used by Yoshida (1992) to model the GDSN *P* waves.

The result is in general agreement with previous estimates of the rupture process obtained from less quantitative analyses of the recorded *P* waves. However, we consider the solution to be unsatisfactory for several reasons. First, the slip history of the *ms*2 precursor is poorly resolved owing both to its smaller amplitude, which results in decreased weighting in the inversion, and to the relatively coarse subfault size used to parameterize the fault. Secondly, the constant rupture-velocity assumption dictates a coherent rupture propagation from the *ms*2 nucleation point and requires that all subsequent seismic radiation correspond to fault locations at prescribed distances from the hypocenter. For earthquakes that involve multiple events occurring at nearby positions on the fault, but at different times, this parameterization yields erroneous distributions of slip (see Mendoza, 1993).

Houston and Kanamori (1990) used the Kikuchi method (Kikuchi and Fukao, 1985) in their finite-fault inversion of the GDSN *P* waves recorded for the Chile earthquake. The method uses an iterative deconvolution procedure to identify the fault locations and times of point-source contributions to the total seismic moment independent of rupture velocity. Their solution shows that *ms*2 contributes little moment compared to the principal moment release that initiates about 16 sec later. This observation is consistent with the interpretation of Choy and Dewey (1988) that *MS* dominates the earthquake rupture process. In this study, we will concentrate further investigation of the 1985 Chile earthquake on the *MS* portion of the recorded waveforms to constrain the location and depth of the principal moment release. In addition, we independently examine the initial failure process of the earthquake by conducting a forward-modeling analysis of the *ms*2 subevent. This subevent was sufficiently well recorded above the noise level at several GDSN stations.

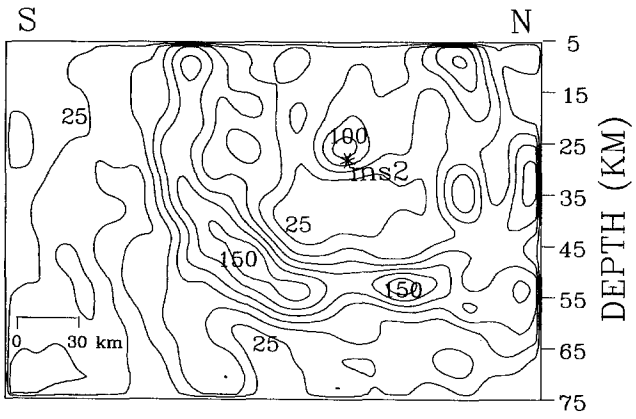

Figure 2. Fault slip inferred from the teleseismic body waves using a fixed rupture velocity of 2 km/sec and record start times corresponding to the arrival of *ms*2. The fault dip is constant (25°), and the nucleation point (asterisk) is located at the downward projection of the *ms*2 epicenter. Coseismic slip is contoured at 25-cm intervals.

From source parameters computed for Chile aftershocks located within 100 km of the trench, Choy and Dewey (1988) suggest that the plate interface dips at an angle of 15° in this region but increases to about 35° landward of this distance. Point-source forward modeling of the intermediate-period, vertical GDSN *P* waves recorded for *ms*2 yields a pure dip-slip thrust mechanism (5° strike, 15° dip) at a depth of 22 km using a 1-2-1 sec trapezoidal source-time function. The corresponding waveform fits are shown in Figure 3. The mechanism, depth, and location of *ms*2 are consistent with shallow-angle thrusting in the updip portion of the plate boundary prior to the principal moment release. Based on this result and on the aftershock analysis of Choy and Dewey (1988), we use a hinged-fault parameterization to study the 1985 Chile earthquake (Fig. 4). The fault has a strike of 5° and consists of two separate segments with different dips and rakes. The upper segment has a dip of 15° and a rake of 90°, consistent with our modeling results for *ms*2 and the aftershock parameters obtained by Choy and Dewey (1988). The dip and rake of the lower segment are 30° and 110°, respectively, consistent with centroid mechanisms obtained for the earthquake. This lower segment contains the *MS* rupture nucleation point at a depth of 40 km. The two fault segments meet at a depth of 26 km with the entire fault covering depths between 6.6 and 71 km. We inverted the *MS* teleseismic body waveforms using 10 time windows, each with a boxcar duration of 2 sec, thus allowing up to 20 sec for the dislocation rise time on the fault.

The inversion (model BW1) produces a lower variance and misfit error than the *ms*2 fixed-velocity run described earlier (see Table 5). Also listed in Table 5 are the results of an additional body-wave time-window inversion where the observed intermediate-period records have been exponentially tapered after 60 sec (model BW2). The majority of the body-wave energy observed

in these records is contained in the first 50 to 60 sec following the arrival of *MS*. The two time-window runs give similar slip patterns, but we consider the second run to provide a better-constrained estimate of the co-seismic slip because it does not attempt to model the latter non-source-related portion of the records. The resulting distribution of slip (Fig. 5) shows several peaks, including a maximum displacement of 2.4 m near the hypocenter and three zones of peak slip in the upper section of the fault. Also shown in Figure 5 is the rise-time function obtained for the maximum slip near the hypocenter. This function suggests a rise time of about 14 sec. Rise-time functions computed for the shallower peaks show similar 14-sec durations. The inferred rupture pattern is consistent with the distribution of mainshock moment release obtained by Houston and Kanamori (1990) using a single planar fault dipping at 30°. Both solutions indicate significant co-seismic rupture along the shallow section of the plate boundary. Also, the deepest point source observed by Houston and Kanamori (1990) is near the *MS* hypocenter at a depth of 40 km.

Surface-Wave Analysis

Our body-wave time-window inversion indicates that the majority of the moment release during the 1985 Chile mainshock (*MS*) occurs in the first 60 sec. This duration is consistent with the *P*-wave results of Houston and Kanamori (1990). Source durations computed for the earthquake using long-period surface waves vary between 60 and 80 sec (see Table 1). The similarity in durations, together with the similarity between our body-wave moment estimate (1.18×10^{28} dyne-cm) and the long-period surface-wave moments listed in Table 1, would suggest that the rupture history of the 1985 Chile earthquake is fairly well explained by the teleseismic body-wave data.

We re-examine the long-period source duration and surface-wave seismic moment of the 1985 Chile earthquake by inverting the full Rayleigh waveforms recorded at the IDA and GEOSCOPE stations assuming a point-source mechanism. In this procedure, we first generate Rayleigh-wave synthetics for a point source with a given

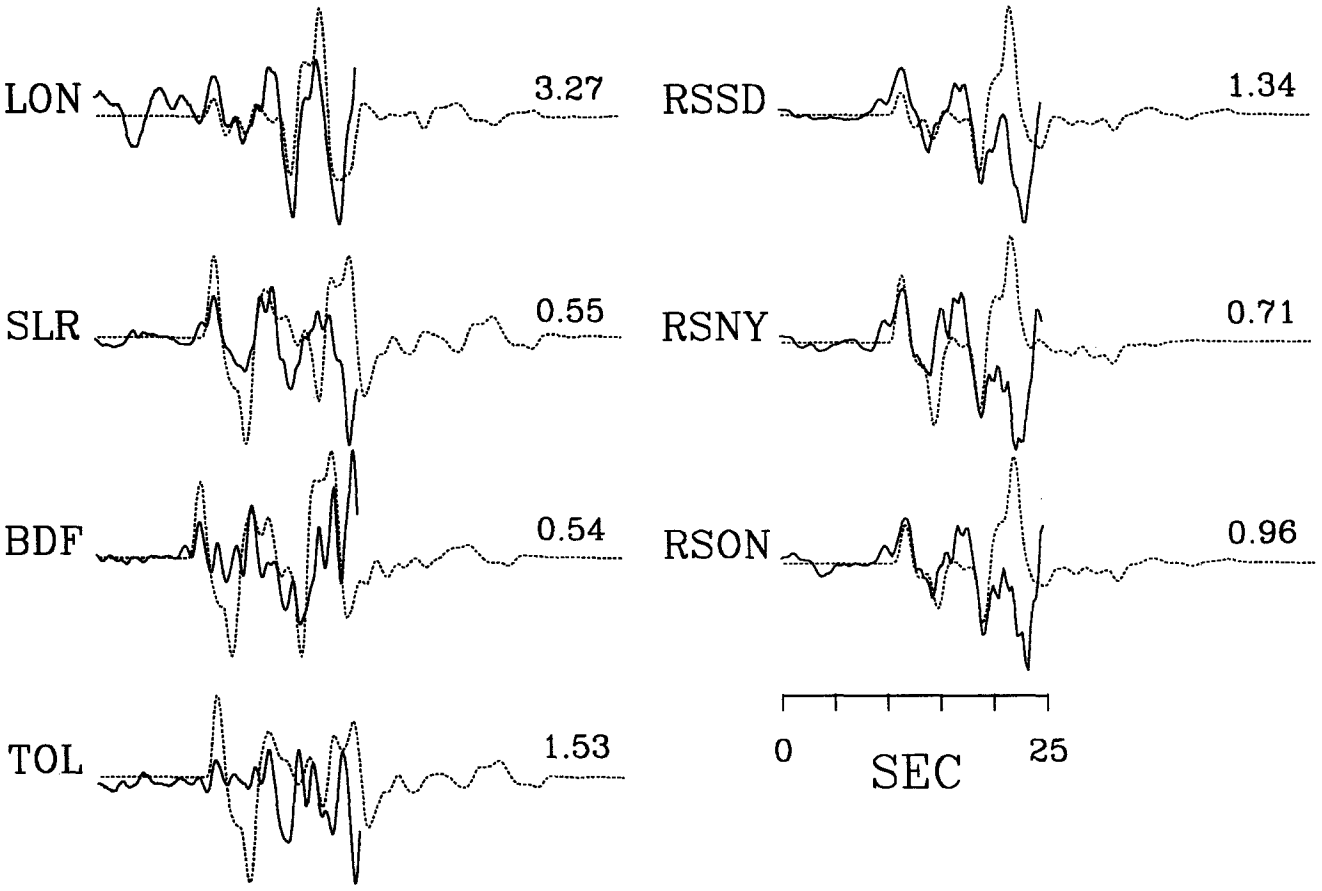

Figure 3. Comparison of the *ms*2 *P* waveforms recorded at the intermediate-period GDSN stations (solid) and synthetic waveforms (dashed) predicted by a point source with 5° strike, 15° dip, 90° rake, 22-km depth, (1-2-1 sec) trapezoidal source-time function, and seismic moment of 1.0×10^{26} dyne-cm. Synthetic-to-observed amplitude ratios are given for each seismogram pair.

source rise time. We then construct a discretized source-time function with time intervals equivalent to the point-source duration and invert the observations to calculate the contribution in each time interval to the total seismic moment. We place the source at the *MS* hypocenter (40-km depth) and assume a 20-sec boxcar for each time window. The strike, dip, and rake of the fault are 5°, 30°, and 110°, respectively. This mechanism is based on the centroid parameters listed in Table 1 and is the same as that used for the lower segment of the hinged fault in our body-wave analysis. Figure 6 shows the results of the inversion. Although the inversion allows up to 400 sec for the source duration, the majority of the long-period moment release occurs within the interval of 20 to 80 sec, consistent with the body-wave results. Contributions to the moment outside of this interval are less than 15% of the peak and are not well resolved. The surface-wave moment in the first 80 sec is 1.2×10^{28} dyne-cm, consistent with previous estimates and almost identical to our body-wave moment.

Inversion of Strong-Motion, Teleseismic, and Surface-Wave Data

We have performed a simultaneous inversion of the teleseismic body waves, long-period surface waves, and local strong motions to further constrain the distribution of mainshock slip for the 1985 Chile earthquake. In our previous body-wave inversion, we used a discretized rise-time function consisting of 2-sec boxcars. Boxcars with a duration greater than 1 sec, however, do not reproduce

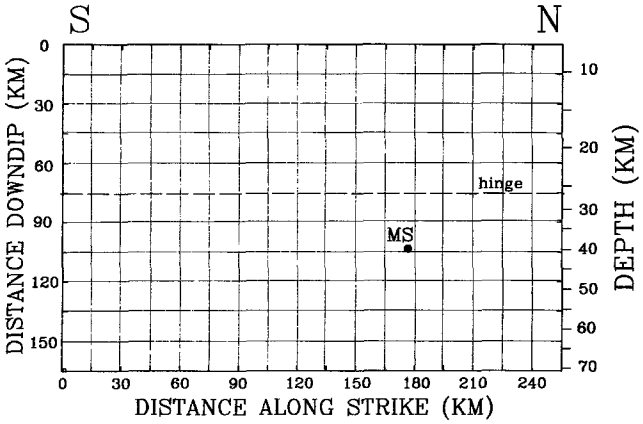

Figure 4. Parameterization of hinged fault used in the time-window analysis of the 1985 Chile earthquake. The fault measures 255 by 165 km and is divided into 187 15- by 15-km subfaults. The upper section above the hinge (dashed line) dips at 15° and is assumed to have a rake of 90°. The lower section has a dip and rake of 30° and 110°, respectively. The nucleation point (filled circle) corresponds to the *MS* hypocenter located by Choy and Dewey (1988).

the high-frequency content present in the strong-motion records, and their inclusion requires us to use a boxcar width of 1 sec or less. Thus, in the joint inversion of all three data types, we apply the variable rise-time approach using a 1-sec duration for each of 14 time windows to allow for the subfault rise time observed in the body-wave analysis. Each of the three data sets is weighted appropriately to prevent any one data type from dominating the result. The results are shown in Figure 7. The pattern is very similar to that obtained using only body waves (Fig. 5), except that peak slips are up to 50 cm greater for several of the source regions. This results in an increased seismic moment of 1.5×10^{28} dyne-cm.

The synthetic waveforms predicted by the slip distribution are compared with the observed seismic data in Figure 8. This comparison indicates that the waveforms considered here, which cover a very wide range of frequencies, can be explained by a single rupture model and do not require a separate longer-duration component of fault motion to reconcile the observed Rayleigh-wave amplitudes. The inferred depth range (10 to 55 km) is consistent with the long-period surface-wave centroid depths computed by Dziewonski *et al.* (1985) and by Zhang and Kanamori (1988a). The results are also generally consistent with the slip pattern obtained by Barrientos (1988) from a finite-fault inversion of the post-seismic elevation changes observed on an east–west line extending from the city of Santiago to the coast. Using a strike of 10° and a rake of 105°, Barrientos (1988) inferred a fault dip of 18° and a seismic moment of 1.6×10^{28} dyne-cm from the geodetic data. The maximum slip (2.6 m) in the geodetic model is at a depth of about 35 km and is located very close to the 2.9-m hypocentral peak observed in our seismic-wave model. Barrientos (1988) observed a second region of large slip about 80 km south of the hypocenter. This second slip region may correspond to the southern source observed in our rupture model, but the geodetic leveling data inverted by Barrientos (1988) may be too far north to fully resolve its location. Also, unlike our solution, the geodetic model does not show significant slip updip of the hypocentral source. The updip slip in our fault model is located up to 75 km seaward of the Chile coast and would thus have little effect on the vertical deformation measurements utilized by Barrientos (1988).

Figure 9 shows the far-field source-time function obtained by integrating our inferred slip distribution across the fault. Also shown in Figure 9 is the time evolution of the co-seismic slip. This rupture history is obtained by calculating the contributions of slip at 5-sec intervals for the 70-sec mainshock duration indicated by the corresponding source-time function. The slip history indicates that mainshock rupture propagated mainly updip from the hypocenter and then moved southward along the shallow-dipping section of the plate boundary. The large source near the hypocenter occurs within the first

15 sec. Rupture then propagates updip toward the trench until about 40 sec into the rupture. The southern source begins to develop after 35 sec of rupture and moves southward along the fault. The majority of the slip occurs in the northern portion of the fault. This spatial distribution of slip is reflected in the mainshock source-time function, which shows the majority of the moment released in the first 40 sec.

Conclusions and Discussion

Several investigators (e.g., Christensen and Ruff, 1986; Korrat and Madariaga, 1986; Choy and Dewey, 1988) have pointed out the multiple-event nature of the 3 March 1985 Chile earthquake. Choy and Dewey (1988) identify two progressively larger precursors prior to the arrival of the principal *P*-wave energy in the recorded GDSN waveforms. From *P*-waveform modeling of the mainshock and large aftershocks, they suggest that the dip of the thrust interface in this portion of the Nazca–South America plate boundary progressively increases landward from about 15° to about 35°. The mainshock hypocenter is on the downdip portion of the plate interface at a depth of 40 km. The larger of the two precursors (*ms*2) precedes the main moment release by about 16 sec and has source parameters similar to those ob-

Table 5
Body-Wave Inversion Results

Run	Moment (dyne-cm)	$\|b - Ax\|$	Variance	Comments
*ms*2	1.45×10^{28}	20.671	0.0613	2 km/sec rupture velocity *ms*2 start times
*BW*1	1.33×10^{28}	19.744	0.0553	10 2-sec time windows *MS* start times
*BW*2	1.18×10^{28}	18.930	0.0496	exponential taper after 60 sec

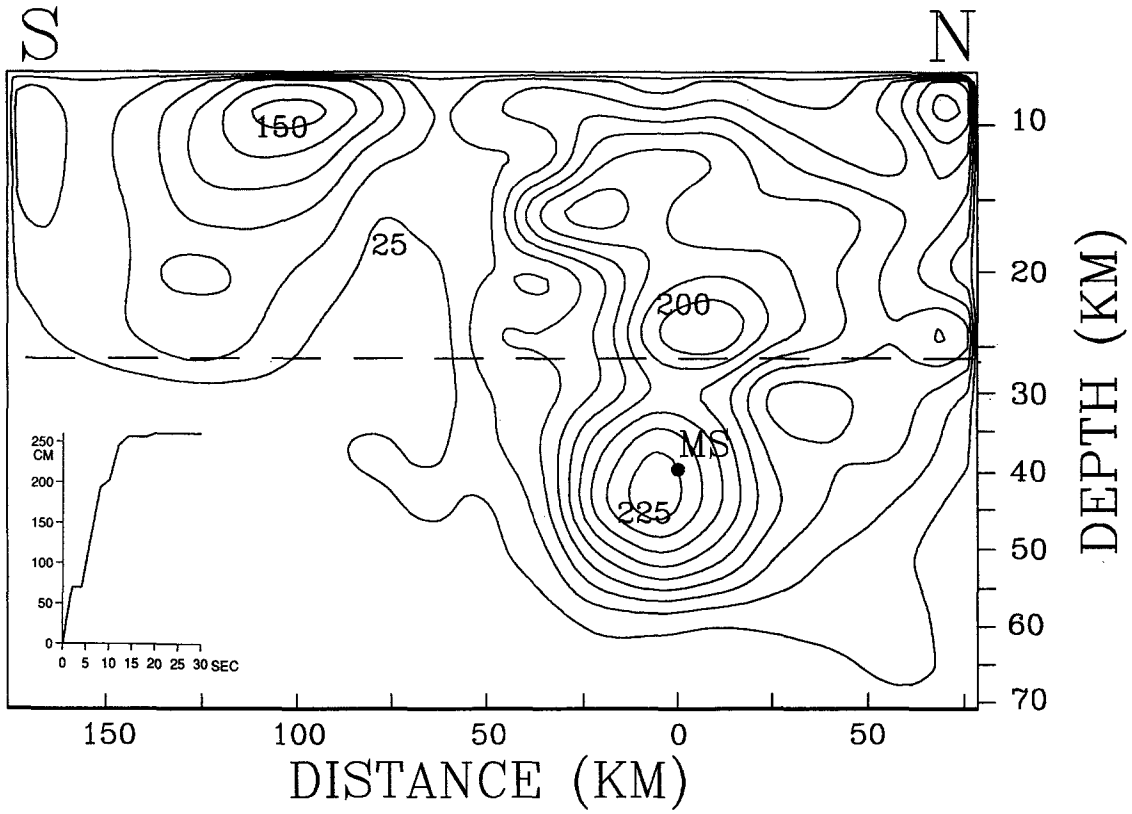

Figure 5. Slip distribution obtained from a variable rise-time inversion of the teleseismic body waves using 10 2-sec time windows. Cumulative slip is contoured at 25-cm intervals and contains all fault displacement occurring within 20 sec after the passage of a rupture front propagating at 3 km/sec away from the hypocenter (filled circle). The dashed line marks where the fault dip changes from 15° to 30°. The inset shows the dislocation rise time observed for the region of maximum slip located near the hypocenter. The other regions of peak slip have similar rise times.

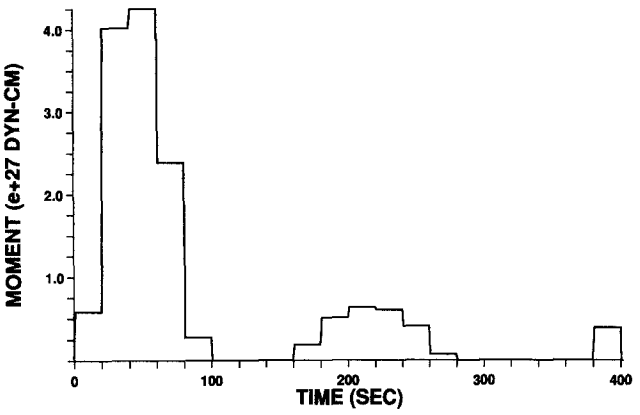

Figure 6. Source-time function of the 1985 Chile earthquake obtained from a point-source analysis of the long-period Rayleigh waves recorded at the GEOSCOPE and IDA stations. Eighty percent of the total seismic moment of 1.5×10^{28} dyne-cm is contained in the first 80 sec.

served by Choy and Dewey (1988) for large aftershocks in the updip portion of the plate interface. Our forward modeling of the intermediate-period, vertical *P* waves recorded for *ms2* suggests a 15° dipping thrust mechanism at a depth of 22 km. The corresponding seismic moment is 1.0×10^{25} dyne-cm. These observations would suggest that the 1985 Chile earthquake began with several precursory events, including a larger ($M_w \sim 6.6$) thrust earthquake at a depth of 22 km, followed by the principal moment release further downdip in the more steeply dipping portion of the plate boundary.

We have examined the local strong ground motions and teleseismic body and surface waves recorded for the earthquake using a variable rise-time finite-fault inversion scheme to recover a detailed rupture history of the principal moment release. In the inversion, we assume a hinged fault with two different dips to simulate the landward increase in plate-boundary dip suggested by Choy and Dewey (1988). We consider this hinged fault to provide a more realistic description of the actual plate geometry in the region. However, modeling the slip distribution on a fault with constant dip would yield a similar rupture pattern and would not change the major conclusions of this study. The teleseismic body-wave data include GDSN *P* and *SH* waves, and the surface waves are *R*1, *R*2, and *R*3 wave trains from the IDA and GEOSCOPE networks. Together with the strong motions, these seismic records contain a wide range of frequencies that include periods from about 2 to 350 sec. The resulting slip distribution explains all three data types equally well. The pattern is very similar to that obtained from a variable rise-time inversion of only the body-wave records, indicating that a significant downdip component of slower fault motion is not required to fully explain the IDA and GEOSCOPE Rayleigh waves. The increased seismic moment (1.5×10^{28} dyne-cm) relative to the body-wave

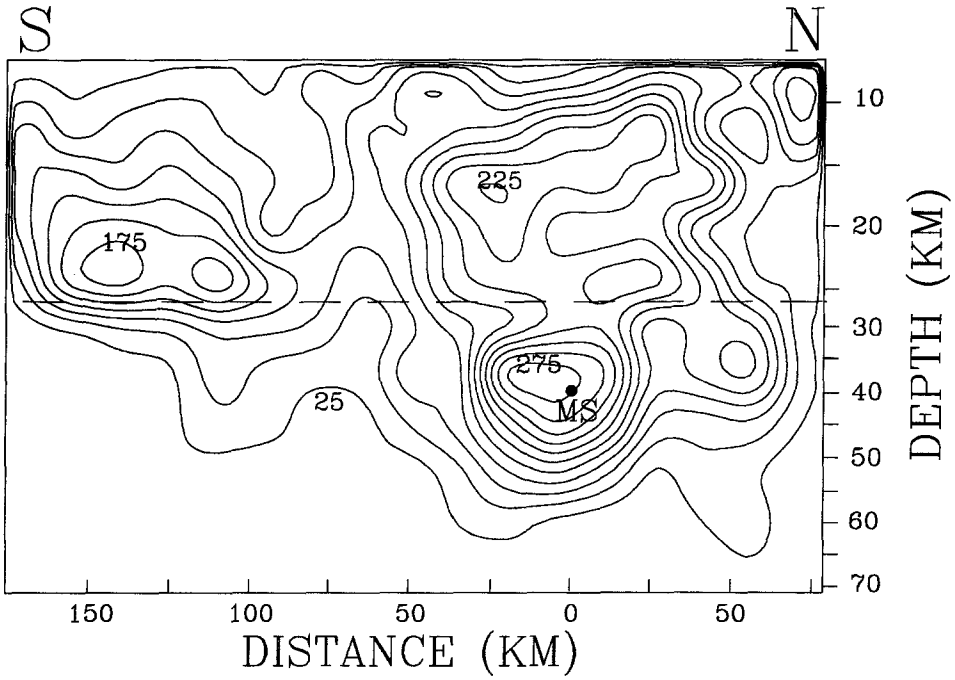

Figure 7. Slip distribution obtained from a time-window inversion of the body-wave, surface-wave, and strong-motion data. Fault slip is contoured at 25-cm intervals 14 sec after the passage of a rupture front propagating at 3 km/sec away from the hypocenter (filled circle). The dashed line marks where the fault dip changes from 15° to 30°.

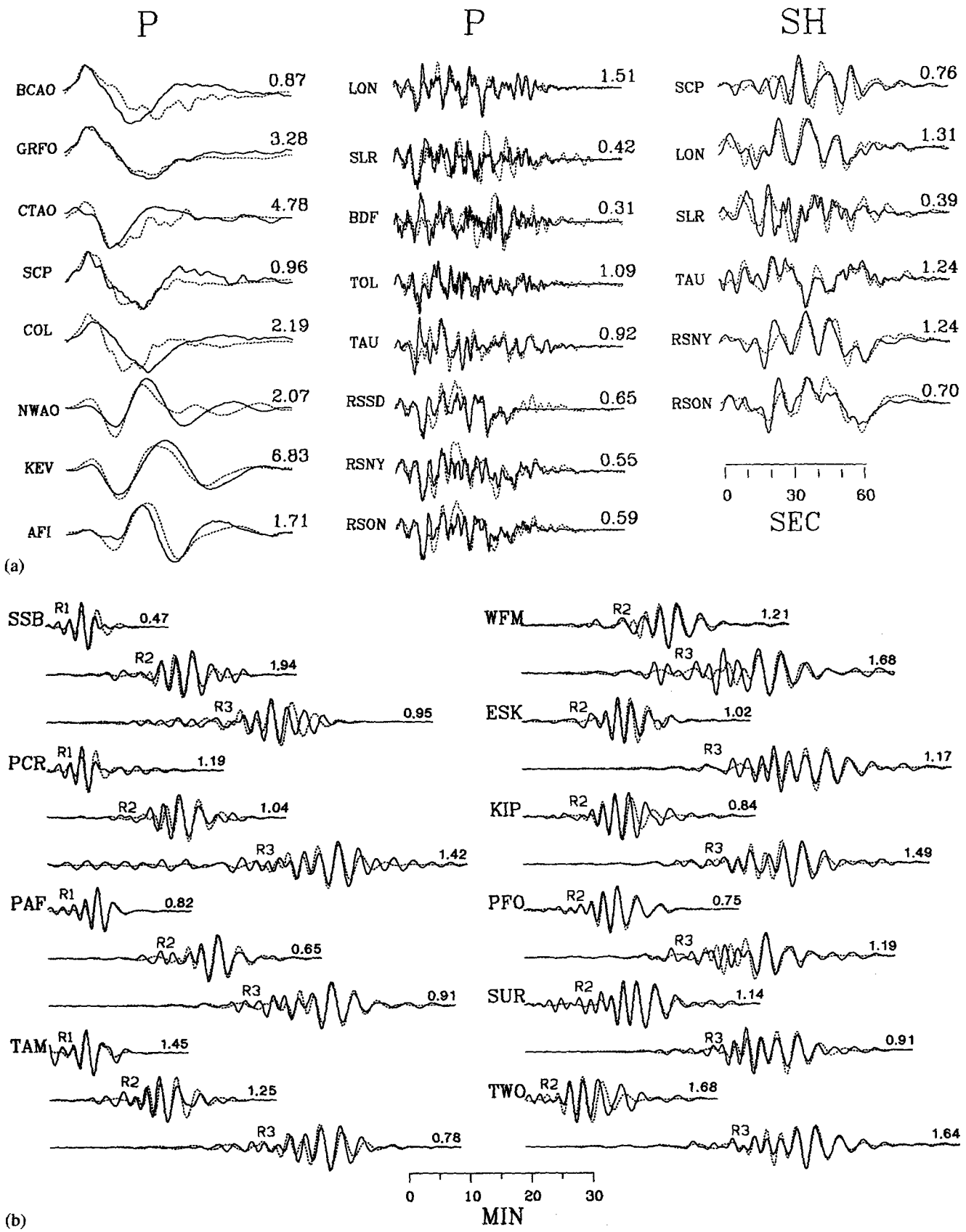

Figure 8. Comparison of observed (solid) and synthetic (dashed) body-wave (a), Rayleigh (b), and strong-motion (c) records for the wide-band source model shown in Figure 7. Synthetic-to-observed amplitude ratios are indicated for each waveform pair.

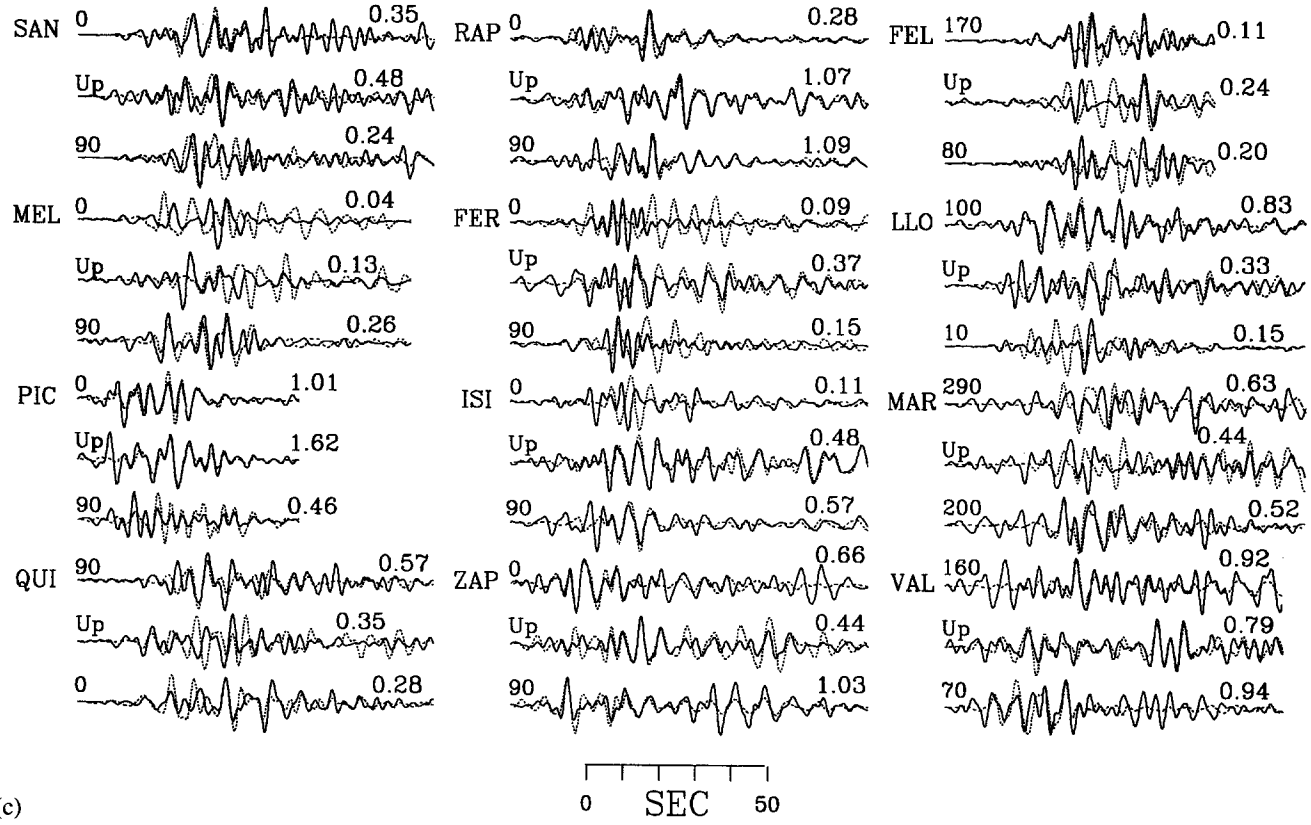

Figure 8—*Continued*

estimate may reflect the band limitation of the body-wave data. The GDSN body waveforms utilized in the inversion are dominated by seismic energy at periods lower than about 30 sec and do not well resolve longer-period excitation that results from fault motion over the entire 200-km length of the fault.

The majority of the moment released during the mainshock is located in the northern half of the fault and covers depths between 10 and 55 km. Peak slips in this region exceed 2 m and include the maximum slip observed for the earthquake, a 2.9-m peak slip near the mainshock hypocenter at a depth of 40 km. A smaller region of lesser slip (1.8-m peak) is also resolvable in the southern portion of the fault. This smaller source is narrower and does not extend deeper than 30 km downdip along the assumed plate interface. The slip pattern indicates that mainshock rupture propagated mainly updip from the hypocenter toward the trench and then laterally to the south along the plate boundary. Distributions of co-seismic slip inferred for other large interplate thrust earthquakes would suggest a similar updip propagation of rupture. Many of the rupture patterns presented by Thatcher (1989) show the earthquake hypocenter located near the downdip edge of the slip region. Precise nucleation points for large subduction earthquakes, however, are difficult to determine, owing to the complicated nature of the *P*-wave arrivals, and the fact that the general characteristics of rupture initiation and propagation at subducting plate boundaries cannot be easily identified. The large $M_w \sim 6.6$ precursor observed for the 1985 Chile earthquake, for example, would suggest a complex mechanism of coherent rupture involving slip in the upper portion of the plate boundary prior to the updip propagation of rupture from the mainshock hypocenter. Alternatively, however, the precursory events may represent foreshocks occurring in separate small regions of the fault where the stress is higher than the local breaking strength (e.g., Das and Scholz, 1981). In this case, the precursors would not be an integral part of the mainshock nucleation process.

Our analysis also indicates that a rise time of about 14 sec is required for regions of maximum slip on the fault. This rise time is longer than that usually considered in body-wave finite-fault inversions but is still short compared to the total source duration of the mainshock (70 sec) and would not necessarily be inconsistent with a propagating-pulse rupture mechanism (e.g., Heaton, 1990) across the entire fault dimensions. However, a 14-sec rise time would also be consistent with the dynamic rupture of a single asperity. Numerical simulations by Day (1982) indicate that, for a square shear crack, the rise time at the center of the fault is approximately equal to the fault length divided by the shear-wave speed. For a 14-sec rise time, the crustal properties listed in Table

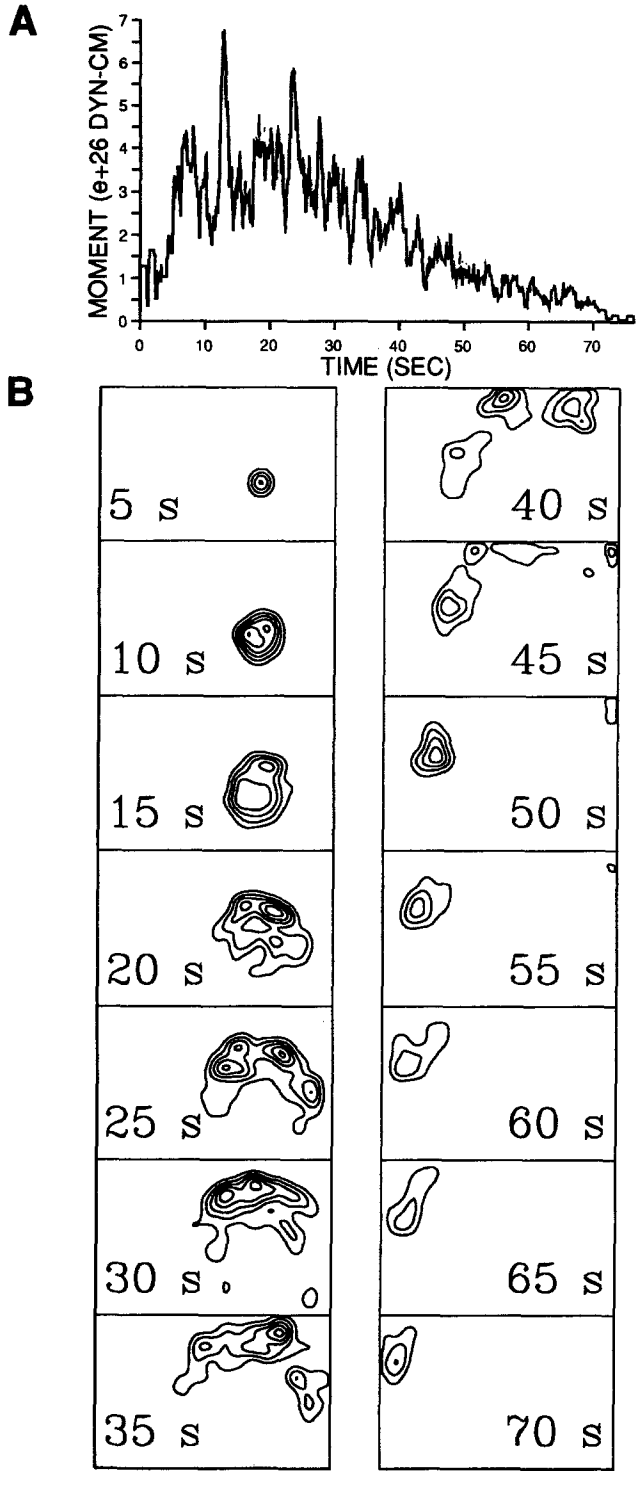

Figure 9. Far-field source-time function (a) and rupture history (b) inferred for the 1985 Chile mainshock. Time frames in (b) show fault-slip distributions at discrete 5-sec intervals beginning at the onset of mainshock moment release. Slips greater than 20 cm are contoured at 20-cm intervals.

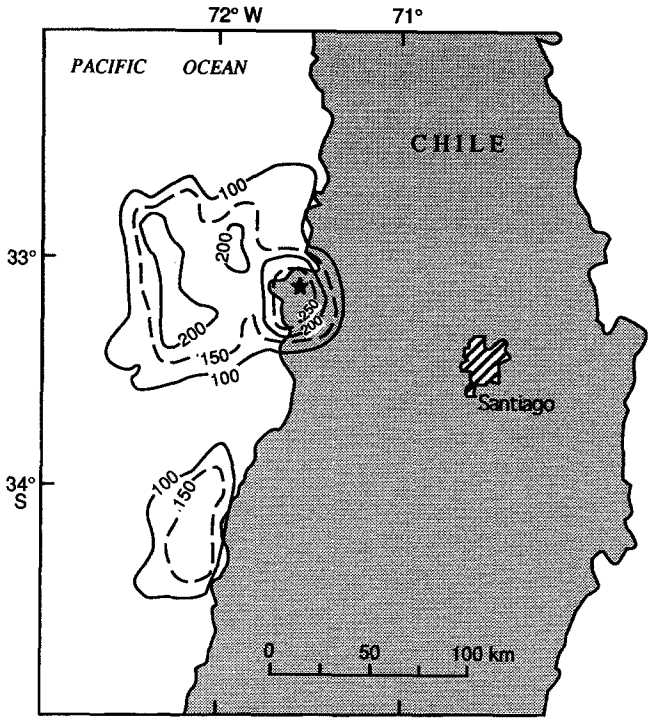

Figure 10. Geographic map of central Chile showing our inferred dislocation model from Figure 7 projected to the surface of the Earth. Slip greater than 1 m is contoured at 50-cm intervals.

4 would suggest a linear dimension of about 50 to 60 km. This dimension agrees very well with the areas of large slip observed for the 1985 Chile earthquake and may indicate that the mainshock involved the dynamic failure of independent asperities distributed along the plate interface. The peak slips observed for these asperity zones would suggest particle velocities on the order of 15 to 20 cm/sec.

The distribution of slip obtained from our wide-band analysis is shown projected onto the Chile coast in Figure 10. The entire 1985 rupture area covers a lateral distance of about 200 km with the large northern source region centered near 33° S latitude. This location has been the epicentral site of several large thrust earthquakes, including the great $M_w \sim 8.5$ earthquake of 16 August 1906 that ruptured from about 32° S to 35° S (Nishenko, 1985; Comte *et al.*, 1986). The rate of relative plate convergence in this region (9 cm/yr) would suggest an accumulation of over 7 m of tectonic slip in the 78.5 yr between the 1906 and 1985 earthquakes. Our inferred maximum slip (2.9 m) is too small to reconcile the accumulation of tectonic strain since 1906 and would suggest that a future large-slip event has yet to occur in the area. However, the 1985 earthquake may have involved a larger peak slip that cannot be fully derived using the smoothing constraints imposed in our inversion. That is, localized peak slips closer to the expected tectonic slip would be smoothed out in the inversion pro-

cess. Nonetheless, the potential is probably high for large earthquake occurrence in the region, considering that the 1985 earthquake covered only a portion of the rupture inferred for the 1906 earthquake. A large M_w 7.8 earthquake occurred on 9 July 1971 within the 1906 rupture zone north of the 1985 earthquake, but the region south of the 1985 zone has not reruptured and may be the most likely site for a future large earthquake (Comte *et al.*, 1986; Christensen and Ruff, 1986).

Acknowledgments

The authors thank Madeleine Zirbes for supplying the GDSN, IDA, and GEOSCOPE data used in the study. Strong-motion records were obtained from the NOAA National Geophysical Data Center in Boulder, Colorado. Sergio Barrientos guided us to the appropriate references for the crustal velocity model, and Heidi Houston provided important details of her finite-fault inversion of the GDSN *P*-wave data. We also thank Jim Dewey for giving us the epicentral coordinates of *ms*1 and *ms*2. Comments by George Choy, Stu Nishenko, and two anonymous reviewers resulted in significant improvement to the manuscript.

References

Anderson, H. J. and J. Zhang (1991). Long-period seismic radiation from the May 23, 1989, Macquarie Ridge earthquake: evidence for coseismic slip in the mantle? *J. Geophys. Res.* **96**, 19853–19863.

Barrientos, S. E. (1988). Slip distribution of the 1985 central Chile earthquake, *Tectonophysics* **145**, 225–241.

Beroza, G. and P. Spudich (1988). Linearized inversion for fault rupture behavior: application to the 1984 Morgan Hill, California earthquake, *J. Geophys. Res.* **93**, 6275–6296.

Campbell, K. W., S. T. Algermissen, E. Kausel, and L. M. Highland (1989). Processed strong-motion data for the central Chile earthquake of March 3, 1985: fifteen accelerograph sites owned by CHILECTRA, ENDESA, and the Department of Geology and Geophysics, University of Chile, *U.S. Geol. Surv. Open-File Rept. 89–448*.

Cara, M. (1973). Filtering of dispersed wavetrains, *Geophys. J. R. Astr. Soc.* **33**, 65–80.

Celebi, M. (1987). Processed Chile earthquake records of 3 March 1985 and aftershocks, *U.S. Geol. Surv. Open-File Rept. 87–195*.

Choy, G. L. and V. F. Cormier (1986). Direct measurement of the mantle attenuation operator from broadband P and S waveforms, *J. Geophys. Res.* **91**, 7326–7342.

Choy, G. L. and J. W. Dewey (1988). Rupture process of an extended earthquake sequence: teleseismic analysis of the Chilean earthquake of March 3, 1985, *J. Geophys. Res.* **93**, 1103–1118.

Christensen, D. H. and L. J. Ruff (1986). Rupture process of the March 3, 1985 Chilean earthquake, *Geophys. Res. Lett.* **13**, 721–724.

Comte, D., A. Eisenberg, E. Lorca, M. Pardo, L. Ponce, R. Saragoni, S. K. Singh, and G. Suarez (1986). The 1985 Central Chile earthquake: a repeat of previous great earthquakes in the region? *Science* **233**, 449–453.

Das, S. and C. H. Scholz (1981). Theory of time-dependent rupture in the Earth, *J. Geophys. Res.* **86**, 6039–6051.

Das, S. and B. V. Kostrov (1990). Inversion for seismic slip rate history and distribution with stabilizing constraints: application to the 1986 Andreanof Islands earthquake, *J. Geophys. Res.* **95**, 6899–6913.

Day, S. M. (1982). Three-dimensional finite difference simulation of fault dynamics: rectangular faults with fixed rupture velocity, *Bull. Seism. Soc. Am.* **72**, 705–727.

Dziewonski, A. M. and D. L. Anderson (1981). Preliminary reference Earth model, *Phys. Earth Planet. Interiors* **25**, 297–356.

Dziewonski, A. M., J. E. Franzen, and J. H. Woodhouse (1985). Centroid-moment tensor solutions for January–March 1985, *Phys. Earth Planet. Interiors* **40**, 249–258.

Fukuyama, E. and K. Irikura (1986). Rupture process of the 1983 Japan Sea (Akita-Oki) earthquake using a waveform inversion method, *Bull. Seism. Soc. Am.* **76**, 1623–1640.

Hartzell, S. H. (1989). Comparison of seismic waveform inversion results for the rupture history of a finite fault: application to the 1986 North Palm Springs, California, earthquake, *J. Geophys. Res.* **94**, 7515–7534.

Hartzell, S. H. and T. H. Heaton (1983). Inversion of strong ground motion and teleseismic waveform data for the fault rupture history of the 1979 Imperial Valley, California, earthquake, *Bull. Seism. Soc. Am.* **73**, 1553–1583.

Hartzell, S. H. and T. H. Heaton (1986). Rupture history of the 1984 Morgan Hill, California, earthquake from the inversion of strong motion records, *Bull. Seism. Soc. Am.* **76**, 649–674.

Hartzell, S. H. and M. Iida (1990). Source complexity of the 1987 Whittier Narrows, California, earthquake from the inversion of strong-motion records, *J. Geophys. Res.* **95**, 12475–12485.

Hartzell, S. H., G. S. Stewart, and C. Mendoza (1991). Comparison of L_1 and L_2 norms in a teleseismic waveform inversion for the slip history of the Loma Prieta, California, earthquake, *Bull. Seism. Soc. Am.* **81**, 1518–1539.

Harvey, D. and G. L. Choy (1982). Broadband deconvolution of GDSN data, *Geophys. J. R. Astr. Soc.* **69**, 659–668.

Heaton, T. H. (1990). Evidence for and implications of self-healing pulses of slip in earthquake rupture, *Phys. Earth Planet. Interiors* **64**, 1–20.

Houston, H. and H. Kanamori (1990). Comparison of strong-motion spectra will teleseismic spectra for three magnitude 8 subduction-zone earthquakes, *Bull. Seism. Soc. Am.* **80**, 913–934.

Kanamori, H. and J. J. Cipar (1974). Focal process of the great Chilean earthquake May 22, 1960, *Phys. Earth Planet. Interiors* **9**, 128–136.

Kausel, E. and J. Cruzat (1985). Regional distribution of Q values from coda waves of local earthquakes in Chile, in *Symposium on Seismic and Volcanic Risk in South America*, **14**, A. Giesecke (Editor), 204–217.

Kikuchi, M. and Y. Fukao (1985). Iterative deconvolution of complex body waves—the Tokachi-Oki earthquake of 1968, *Phys. Earth Planet. Interiors* **37**, 235–248.

Korrat, I. and R. Madariaga (1986). Rupture of the Valparaiso (Chile) gap from 1971 to 1985, in *Earthquake Source Mechanics*, S. Das, J. Boatwright, and C. H. Scholz (Editors), Geophysical Monograph 37, Am. Geophys. Union, Washington, D.C., 247–258.

Langston, C. A. and D. V. Helmberger (1975). A procedure for modelling shallow dislocation sources, *Geophys. J. R. Astr. Soc.* **42**, 117–130.

Mendoza, C. (1993). Coseismic slip of two large Mexican earthquakes from teleseismic body waveforms: Implications for asperity interaction in the Michoacan plate-boundary segment, *J. Geophys. Res.* **98**, 8197–8210.

Mendoza, C. and S. H. Hartzell (1988). Inversion for slip distribution using teleseismic P waveforms: North Palm Springs, Borah Peak, and Michoacan earthquakes, *Bull. Seism. Soc. Am.* **78**, 1092–1111.

Mendoza, C. and S. H. Hartzell (1989). Slip distribution of the 19 September 1985 Michoacan, Mexico, earthquake: near-source and teleseismic constraints, *Bull. Seism. Soc. Am.* **79**, 655–669.

Monfret, T. and B. Romanowicz (1986). Importance of on-scale ob-

servations of first-arriving Rayleigh wave trains for source studies: example of the Chilean event of March 3, 1985 observed on the GEOSCOPE and IDA networks, *Geophys. Res. Lett.* **13**, 1015–1018.

Mori, J. and K. Shimazaki (1985). Inversion of intermediate-period Rayleigh waves for source characteristics of the 1968 Tokachi-Oki earthquake, *J. Geophys. Res.* **90**, 11374–11382.

Nishenko, S. P. (1985). Seismic potential for large and great interplate earthquakes along the Chilean and southern Peruvian margins of South America: a quantitative reappraisal, *J. Geophys. Res.* **90**, 3589–3615.

Oppenheim, A. V. and R. W. Schafer (1975). *Digital Signal Processing*, Prentice-Hall, Inc., Englewood Cliffs, New Jersey.

Pardo, M. and A. Fuenzalida (1988). Estructura cortical y subduccion en Chile central, *V Congreso Geologico Chileno, 2*, Santiago, Chile.

Saikia, C. K. and L. J. Burdick (1991). Fine structure of P_{nl} waves from explosions, *J. Geophys. Res.* **96**, 14383–14401.

Takeo, M. (1987). An inversion method to analyze the rupture processes of earthquakes using near-field seismograms, *Bull. Seism. Soc. Am.* **77**, 490–513.

Thatcher, W. (1989). Earthquake recurrence and risk assessment in circum-Pacific seismic gaps, *Nature* **341**, 432–434.

Wald, D. J., D. V. Helmberger, and S. H. Hartzell (1990). Rupture process of the 1987 Superstition Hills earthquake from the inversion of strong-motion data, *Bull. Seism. Soc. Am.* **80**, 1079–1098.

Yoshida, S. (1986). A method of waveform inversion for earthquake rupture process, *J. Phys. Earth* **34**, 235–255.

Yoshida, S. (1992). Waveform inversion for rupture process using a non-flat seafloor model: application to 1986 Andreanof Islands and 1985 Chile earthquakes, *Tectonophysics* **211**, 45–59.

Zhang, J. and H. Kanamori (1988a). Depths of large earthquakes determined from long-period Rayleigh waves, *J. Geophys. Res.* **93**, 4850–4868.

Zhang, J. and H. Kanamori (1988b). Source finiteness of large earthquakes measured from long-period Rayleigh waves, *Phys. Earth Planet. Interiors* **52**, 56–84.

Zhang, J. and T. Lay (1989). A new method for determining the long-period component of the source time function of large earthquakes, *Geophys. Res. Lett.* **16**, 275–278.

U.S. Geological Survey
P. O. Box 25046, MS967
Denver Federal Center
Denver, Colorado 80225
(C.M., S.H.)

mission ORSTOM
Casilla 53390
Correo Central
Santiago 1, Chile
(T.M.)

Manuscript received 18 January 1993.